Journal of Computational Physics 227 (2008) 8807–8819

Contents lists available at ScienceDirect

Journal of Computational Physics

journal homepage: www.elsevier.com/locate/jcp

A boundary-integral model for drop deformation between two parallel plates with non-unit viscosity ratio drops

P.J.A. Janssen, P.D. Anderson *

Materials Technology, Dutch Polymer Institute, Eindhoven University of Technology, P.O. Box 513, 5600 MB, Eindhoven, The Netherlands

ARTICLE INFO

Article history:
Received 21 September 2007
Received in revised form 20 May 2008
Accepted 23 June 2008
Available online 3 July 2008

Keywords:
Viscous drops
Confinements
Boundary-integral method

ABSTRACT

A boundary-integral method is presented for drop deformation between two parallel walls for non-unit viscosity ratio systems. To account for the effect of the walls the Green's functions are modified and all terms for the double-layer potential are derived. The full three-dimensional implementation is validated, and the model is shown to be accurate and consistent. The method is applied to study drop deformation in shear flow. An excellent match with small-deformation theory is found at low capillary numbers, and our results match with other BIM simulations for pressure-driven flows. For shear flow with moderate capillary numbers, we see that the behavior of a low-viscosity drop is similar to that of drop with a viscosity ratio of unity. High-viscosity drops, on the other hand, are prevented from rotating in shear flow, which results in a larger deformation, but less overshoot in the drop axes is observed. In contrast with unconfined flow, high-viscosity drops can be broken in shear flow between parallel plates; for low-viscosity drops the critical capillary number is higher in confined situations.

1. Introduction

Wall interactions can play a major role in the behavior of multiphase systems in microfluidic devices [1–3]. Examples of related problems are the flow through porous media [4], and the behavior of red blood cells in arteries [5,6]. One particular situation that has received considerable attention recently, is the flow of blends or single drops between parallel walls. Blends in shear flow between two parallel plates have been studied by Migler and co-workers [7–9]. The behavior of individual drops in confined geometries was investigated as well [10]. In these experiments, the drop always had the same viscosity as the matrix fluid. Experimental studies which includes the effect of the viscosity ratio in particular have been done on the structure development in a blend [11], the steady-state and transient data [12], and the break-up behavior [13]. Some interesting effects in this latter study were found: break-up is enhanced for high-viscosity drops, while it is suppressed for low-viscosity drops. For viscosity ratios close to unity, the effect of the confinement on the critical capillary number is minor.

Several numerical methods have been used in the past to study the behavior of multiphase systems in the presence of solid boundaries. Examples include volume-of-fluid [14,15], Lattice Boltzmann [16], finite difference [17], finite element [18], and boundary-integral methods with various ways of handling the solids [19–26]. An advantage of the volume-of-fluid type of models is that they are able to include inertia and non-linear viscoelastic behavior [15]; a clear disadvantage is that a full three-dimensional problem needs to be solved, limiting the number of nodes needed to accurately describe a deforming interface. Boundary-integral methods for bulk flows have the advantage that only the drop surface needs to be meshed, which allows for a highly accurate description of the drop. Depending on how the solid is incorporated in the method, it also

* Corresponding author. Tel.: +31 402474823; fax: +31 402447355.
E-mail address: p.d.anderson@tue.nl (P.D. Anderson).

0021-9991/$ - see front matter © 2008 Elsevier Inc. All rights reserved.
doi:10.1016/j.jcp.2008.06.027

needs to be meshed. Nevertheless, the advantage remains that only the shape of the solids needs to be taken into account, and not the whole domain. Another advantage of the boundary-integral model over the volume-of-fluid approach is that thin regions between the drop and the walls are better resolved. Recent advancements for boundary-integral methods include efficient remesh algorithms to handle deforming drops [27,28], multipole acceleration techniques to simulate a vast number of drops [29–31], and implicit time integration schemes [32], all which add to the attractiveness of this method.

In this paper, we build on a previous developed boundary-integral method [33] for drops between two parallel plates which is limited to the unit viscosity case. In that work, the Green's functions used in the boundary-integral formulation were modified to obey the no-slip condition at the wall [34,35]. To take into account a non-unit viscosity ratio, the Green's functions associated with the pressure and stress field also need to be modified. The derivation as well as the numerical evaluation of these terms is outlined in this paper. We then apply the method to study drop deformation in Poiseuille and shear flow, with varying capillary numbers and confinement and viscosity ratios.

2. Mathematical formulation

We consider a drop with radius R in creeping flow conditions between parallel walls, with the walls located at $z = \pm W$, as schematically shown in Fig. 1, where the drop viscosity is given by μ_1, the matrix viscosity by μ_0, and the viscosity ratio λ by μ_1/μ_0. All length scales are scaled with R, time with $\dot\gamma$, velocities with $R\dot\gamma$ and pressures with σ/R, with $\dot\gamma$ the shear rate and σ the interfacial tension. Due to this scaling, the two other parameters that characterize the flow problem, besides λ, are the confinement ratio R/W, and the capillary number $Ca = R\dot\gamma\mu_0/\sigma$.

The discontinuity in the normal stress across the interface is given by $\mathbf{f}$, which reads in non-dimensional form:

$$\mathbf{f}(\mathbf{x}) = \frac{2}{Ca}\kappa(\mathbf{x})\mathbf{n}(\mathbf{x}), \tag{1}$$

with $\mathbf{n}$ the vector normal to the interface, and κ the local curvature. Note that $\mathbf{f}$ only includes the capillary pressure, but the model is easily extended to include van der Waals forces or gradients in interfacial tension [36].

A boundary-integral method [37,38] is used, where the velocity $\mathbf{u}$ at the pole $\mathbf{x}_0 = (x_0, y_0, z_0)^{\mathrm{T}}$ is given by

$$(\lambda+1)\mathbf{u}(\mathbf{x}_0) = 2\mathbf{u}_\infty(\mathbf{x}_0) - \frac{1}{4\pi}\int_S \mathbf{f}(\mathbf{x})\cdot\mathbf{G}(\mathbf{x},\mathbf{x}_0)\,\mathrm{d}S(\mathbf{x}) - \frac{\lambda-1}{4\pi}\int_S \mathbf{u}(\mathbf{x})\cdot\mathbf{T}(\mathbf{x},\mathbf{x}_0)\cdot\mathbf{n}(\mathbf{x})\,\mathrm{d}S(\mathbf{x}). \tag{2}$$

The requirement that the velocity components should vanish at the wall, is obeyed by modifying the Green's functions $\mathbf{G}$ and $\mathbf{T}$ to include the free-space result and a part with the additional contributions due to the presence of the walls:

$$\mathbf{G} = \mathbf{G}^\infty + \mathbf{G}^{2W}; \qquad \mathbf{T} = \mathbf{T}^\infty + \mathbf{T}^{2W}, \tag{3}$$

where the free-space parts are given by

$$\mathbf{G}^\infty(\mathbf{x},\mathbf{x_0}) = \frac{\mathbf{I}}{|\hat{\mathbf{x}}|} + \frac{\hat{\mathbf{x}}\hat{\mathbf{x}}}{|\hat{\mathbf{x}}|^3}, \qquad \mathbf{T}^\infty(\mathbf{x},\mathbf{x_0}) = -6\frac{\hat{\mathbf{x}}\hat{\mathbf{x}}\hat{\mathbf{x}}}{|\hat{\mathbf{x}}|^5}, \tag{4}$$

with $\hat{\mathbf{x}} = \mathbf{x} - \mathbf{x}_0$, and $\mathbf{x} = (x, y, z)^{\mathrm{T}}$ the field point.

The wall contribution of the single-layer potential has been derived by Liron and Mochon [34] and by Jones [35]; in this work we used the latter formulation, since it yields a more symmetric form:

$$G^{2W}_{xx} = -\frac{1}{2}\int_0^\infty \left(J_0(qs) + \frac{\hat y^2 - \hat x^2}{s^2}J_2(qs)\right)t_{1pp}(q,z,z_0)\,\mathrm{d}q + \int_0^\infty J_0(qs)r_{1pp}(q,z,z_0)\,\mathrm{d}q, \tag{5}$$

$$G^{2W}_{zz} = \int_0^\infty J_0(qs)t_{1nn}(q,z,z_0)\,\mathrm{d}q, \tag{6}$$

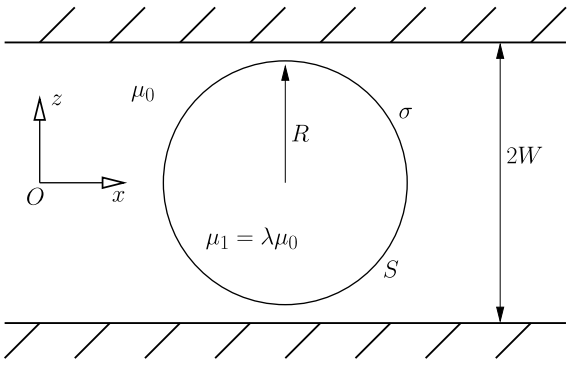

Fig. 1. Schematic representation of a drop with radius R and vicosity μ_1 in a matrix fluid with viscosity μ_0 located between two parallel plates with a distance between the plates of $2W$. The interface is given by S and has an interfacial tension σ.

$$G_{xy}^{2W} = \frac{\hat{x}\hat{y}}{s^2}\int_0^\infty J_2(qs)t_{1pp}(q,z,z_0)\,\mathrm{d}q, \tag{7}$$

$$G_{xz}^{2W} = -\frac{\hat{x}}{s}\int_0^\infty J_1(qs)t_{1pn}(q,z,z_0)\,\mathrm{d}q, \tag{8}$$

$$G_{zx}^{2W} = -\frac{\hat{x}}{s}\int_0^\infty J_1(qs)t_{1np}(q,z,z_0)\,\mathrm{d}q, \tag{9}$$

with $s = \sqrt{\hat{x}^2+\hat{y}^2}$, $\hat{x} = x - x_0$, $\hat{y} = y - y_0$, and J_v is a Bessel function of the first kind with order v. The integrands $t_{1nn},\ldots,r_{1pp}$ can be found in Appendix A. The component G_{yy}^{2W} is the same as G_{xx}^{2W}, with the change $\hat{x}\to\hat{y}$, $\hat{y}\to-\hat{x}$, G_{yz}^{2W} is the same as G_{xz}^{2W} with the factor $\hat{x}$ replaced by $\hat{y}$; the same change goes for G_{zx}^{2W}, and $G_{yx}^{2W} = G_{xy}^{2W}$.

The double-layer potential $\mathbf{T}$ is defined as [38]

$$T_{ijk} = -\delta_{ik}Q_j(\mathbf{x},\mathbf{x}_0) + \frac{\partial G_{ij}}{\partial x_k}(\mathbf{x},\mathbf{x}_0) + \frac{\partial G_{kj}}{\partial x_i}(\mathbf{x},\mathbf{x}_0), \tag{10}$$

where $\mathbf{Q}(\mathbf{x},\mathbf{x}_0)$ is the pressure vector associated with the Green's function $\mathbf{G}$. Similar as for the Green's functions for the velocity and stress, the pressure vector can also be decomposed in a free-space result and a wall contribution, where the components are given by [38,35,39]

$$\mathbf{Q}^\infty(\mathbf{x},\mathbf{x}_0) = 2\frac{\hat{\mathbf{x}}}{|\hat{\mathbf{x}}|^3}, \tag{11}$$

$$Q_x^{2W}(W,\mathbf{x},\mathbf{x}_0) = 2\frac{\hat{x}}{s}\int_0^\infty qJ_1(qs)p_{1p}\,\mathrm{d}q, \tag{12}$$

$$Q_z^{2W}(W,\mathbf{x},\mathbf{x}_0) = 2\int_0^\infty qJ_0(qs)p_{1n}\,\mathrm{d}q, \tag{13}$$

and Q_y^{2W} is the same as Q_x^{2W} with $\hat{x}$ replaced by $\hat{y}$. The integrands p_{1p} and p_{1n} are listed in Appendix A.

To properly evaluate $\mathbf{T}^{2W}$, the partial derivatives of $\mathbf{G}^{2W}$ to $\mathbf{x}$ need to be determined as well. Here, we split them in two different categories: derivatives with respect to z, and those to x and y. The derivatives with respect to z are quite simple: in the terms $t_{1nn},\ldots,r_{1pp}$ (Appendix A), we make the following changes:

$w\cosh(w) \to q[\cosh(w) + w\sinh(w)]$,
$w\sinh(w) \to q[\sinh(w) + w\cosh(w)]$,
$\cosh(w) \to q\sinh(w)$,
$\sinh(w) \to q\cosh(w)$.

The derivatives with respect to x and y require proper differentiation of the Bessel functions:

$$\frac{\partial J_v(qs)}{\partial x} = \frac{\partial s}{\partial x}\frac{\partial J_v(qs)}{\partial s}, \tag{14}$$

where we used the following formulations for the derivatives of the Bessel functions [40]:

$$\frac{\partial J_0(qs)}{\partial s} = -qJ_1(qs); \quad \frac{\partial J_1(qs)}{\partial s} = \frac{1}{2}q(J_0(qs) - J_2(qs)); \quad \frac{\partial J_2(qs)}{\partial s} = qJ_1(qs) - \frac{2}{s}J_2(qs). \tag{15}$$

The eventual expression for a derivative to x or y can be quite long, so here only one result is shown, all the others can be found in Appendix C. The derivative of G_{xz}^{2W} to x is

$$\{G_{xz}^{2W}\}^{(x)} = -\left\{\frac{\hat{x}}{s}\right\}^{(x)}\int_0^\infty J_1(qs)t_{1pn}\,\mathrm{d}q - \frac{x}{s}\{s\}^{(x)}\frac{1}{2}\int_0^\infty q(J_0(qs) - J_2(qs))t_{1pn}\,\mathrm{d}q, \tag{16}$$

where $\{\}^{(x)}$ is the derivative of that term to x.

3. Numerical implementation and validation

The numerical evaluation of the individual terms of the double-layer potential is similar to those of the single-layer potential [22,33]: each integral is split in a part that is handled numerically and one that is handled analytically:

$$\int_0^\infty J_0(qs)t_{1nn}\,\mathrm{d}q = \int_0^\xi J_0(t_{1nn} - \breve{t}_{1nn})\,\mathrm{d}q + \int_0^\infty J_0(qs)\breve{t}_{1nn}\,\mathrm{d}q, \tag{17}$$

where $\breve{t}_{1nn}$ is an approximation of t_{1nn} at high q (see Appendix B for all terms). The second integral of the right-hand side of Eq. (17) can be evaluated analytically. We have made a small modification in $\breve{t}$ compared to [33]: the new terms also include the parts with $\exp(-2qW)$ of $A_+,\ldots,D_-$. The advantage of this is that in this formulation $t - \breve{t}$ is the same as t with $E_\pm$ replaced by $E_\pm - 4\exp(-2qW)$. This works for all terms except t_{1pp} and $t_{1pp}^{(z)}$, but this can be solved by adding two additional

terms (see the end of Appendix B). The integration can be performed much faster this way, as $\breve{t}$ does not have to be evaluated anymore. The rate of decay of $t-\breve{t}$ is now predominately given by $qW\exp(-2qW)$, which decays fast, so performing the numerical integration only from 0 to ξ is sufficiently accurate, where here we have cut off the integration at $\xi=7$. An additional modification to [33], is that a Gaussian integration scheme is used, where only 30 integration points are required, instead of 80–120 points used in a Simpson integration scheme to reach the same level of accuracy. The split of the integration domain is also no longer used, as the current integration scheme was found to be accurate enough.

The derivation and implementation are validated by placing the field point on the wall, and the source point at various locations. In this situation, as the velocity is $\mathbf{0}$ at the wall, $\mathbf{T}^{2W}=-\mathbf{T}^{\infty}$. Convergence with the number of Gauss points and increasing s is shown in Fig. 2. The error decreases rapidly, but increases for larger s. Hence, 30 Gauss points clearly provide accurate results for all situations considered. However, for even larger values of s, this might not be sufficient.

However, large values of s can be tackled in another way. To limit the number of Fourier–Bessel integrals that have to be evaluated, we use an asymptotic expression for the Green's functions at high s. At high s, $\mathbf{G}$ is given by [34,41]

$$\mathbf{G}=\frac{3}{2s^4W^3}(W^2-z^2)(W^2-z_0^2)\begin{pmatrix}\hat{x}^2-\hat{y}^2 & 2\hat{x}\hat{y} & 0\\ 2\hat{x}\hat{y} & \hat{y}^2-\hat{x}^2 & 0\\ 0 & 0 & 0\end{pmatrix}+\mathrm{O}(\mathrm{e}^{-s/2W}). \tag{18}$$

Similarly, the pressure at high s is

$$\mathbf{Q}=\frac{3}{s^2W^3}(W^2-z_0^2)(\hat{x},\hat{y},0)+\mathrm{O}(\mathrm{e}^{-s/2W}). \tag{19}$$

So if s is sufficiently large compared to the wall spacing, the asymptotic formulation can be used. We have chosen the cut-off point at 2.5 wall spacings, or $5W$. Using Eq. (10), the asymptotic expression of $\mathbf{T}$ can be found as well.

Further reduction of the computation time can be achieved by replacing the 2-wall kernel by the summation of the two single-wall kernels, as done by Griggs et al. [26], and possible an additional Taylor expansion for the missing 2-wall part. These authors reported only small differences ($\sim$1%) between two single-wall kernels, and the full Green's function. This has the advantage that no expensive Fourier–Bessel integrals have to be evaluated. This approximation worked well in that case of pressure-driven flow with modest capillary numbers, and indeed, we found similar results (see Section 4.2), but we found serious discrepancies for shear driven flows. In Fig. 3 the additional deformation due to the walls is plotted, for two different ways of handling the 2-wall contribution to the kernels: our current method with the exact Fourier–Bessel integrals, and the summation of two single-wall kernels, given by [42]. With increasing the confinement ratio, the match becomes worse, ultimately leading to break-up for the 2-wall kernel computation, where stable shapes are found for the Fourier–Bessel method. Adding the Taylor expansion, derived by [26], might reduce this error, but we choose not to pursue in that direction, as the current results are accurate enough, and the computational resources required are modest.

The total computation time in evaluating T^{2W} is not much larger compared with G^{2W}. This is mainly due to the fact that the most expensive computation is that of $t_{1nn},\ldots,r_{1pp}$, which has to be done anyhow for G^{2W}. The terms $t^z_{1nn},\ldots,r^z_{1pp}$ and p_{1n} and p_{1p} can be computed quite easily, since the terms independent of w have been evaluated once already.

The other numerical details of our implementation do not differ from previous work [33,43]. A non-singular contour integration is used for the free-space kernels. This split might give problems with the asymptotic formulation we use for the far-field, as they are for full Green's function. As we split the Green's functions in a free-space and a wall contribution part, the free-space Green's function has to be subtracted from the asymptotic one in our implementation. This leads to small numerical errors, where the free-space part is subtracted in a surface integration formulation, and added later in a contour-inte-

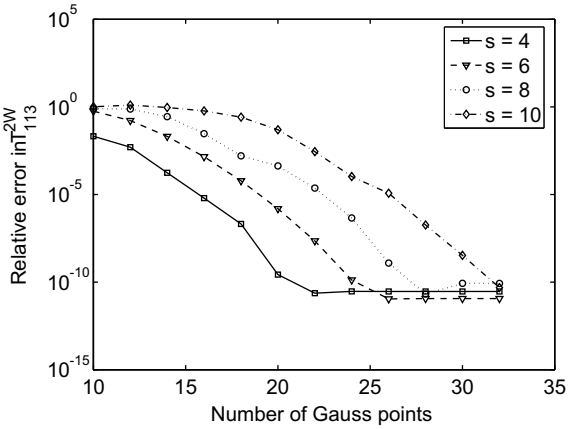

Fig. 2. The relative error in the value of T^{2W}_{113} as function as the number of Gauss points for various values of s.

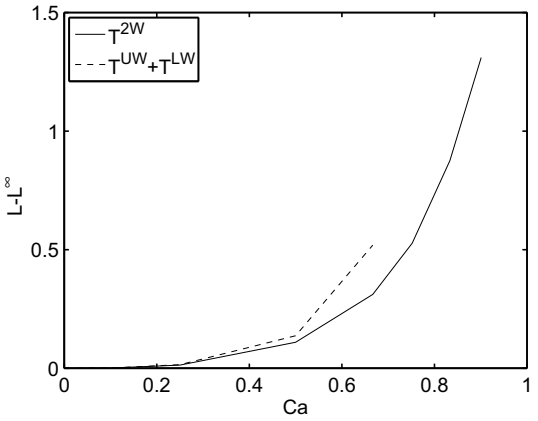

Fig. 3. The additional deformation of the major drop axis due to the presence of the walls as function of the confinement ratio with two methods of calculating the modified Green's functions. These are the stable values for $Ca = 0.3$ and $\lambda = 10$. Computing the modified Green's function with the superposition of the upper and the lower wall kernel led to break-up for higher confinement ratios.

Table 1
Convergence of the major drop axis L with $Ca = 0.2$, $R/W = 0.8$ and $\lambda = 0.1$

	# nodes						
	642	1002	1442	1962	2562	3242	4002
Maximum of L	2.7739	2.7545	2.7445	2.7386	2.7349	2.7323	2.7306
Stable value of L	2.7255	2.7091	2.7030	2.6991	2.6963	2.6942	2.6928

gration representation. The errors are relatively small in our case for studying the transient motion of drops, but could be significant when investigating the far-field velocity field in detail for example, where resulting velocities are small.

Time integration is conducted with a multi-time-step scheme, where the kernels are only evaluated every 50 time steps. A typical time step used was 5×10^{-4} to 1×10^{-3}, depending mainly on the capillary number. Furthermore, the curvature and normal vector were evaluated via contour-integration [44]. The iterative procedure to solve for $\mathbf{u}$ in Eq. (2) is done via simple successive substitution. Except for the initial time step, all steps require no more then 3 iterations, so we found no need to use more advanced solving procedures, as for example a bi-conjugate gradient method [45]. Each time step, the uniform drop expansion is removed from the solution spectrum. Finally, the mesh is updated with the normal component of the interfacial velocity in addition to an extra tangential velocity that moves nodes to places with high curvature [44]. As deformations were limited, no remesh algorithm [27,28] was used, except for studying the break-up modes.

Finally, we show consistency with the number of nodes N. For this case we consider the deformation of a drop in shear flow, with $Ca = 0.2$, $R/W = 0.8$ and $\lambda = 0.1$, for which we focus on the major axis L, defined as the largest distance between two nodes. Besides L, we also define B as twice the minimum distance from the mass center of the drop to the interface, and L_W as maximum size in the xy-plane. In Table 1, L is shown with the stationary value and the highest transient value for a varying number of nodes. It is clear that we reach a converged result. As a boundary-integral method is only first-order accurate in N, the convergence is slow, but sufficient for the accuracy we are aiming for. In the following simulations, 4002 nodes were used.

4. Results

In this section, our method is applied to study the deformation of a drop in shear and Poiseuille flow between two parallel walls. In particular the influence of the viscosity ratio is investigated. First we compare our results with a small-deformation theory, then we compare results published for a pressure-driven problem, and then we investigate the influence of the viscosity ratio on the deformation of the drops for modest capillary numbers. Finally, we show break-up for a high-viscosity drop in shear flow.

4.1. Comparison with small-deformation theory

Similar as has been done in previous experimental [10] and numerical [33] work, we compare our results with the small-deformation theory of Shapira and Haber [46], which describes the enhanced deformation of the drop, expressed in the Taylor deformation parameter $D = (L - B)/(L + B)$, as

$$D^{2W} = Ca\left(\frac{R}{2W}\right)^3 \frac{1+2.5\lambda}{1+\lambda}\frac{16+19\lambda}{8(1+\lambda)}\sin(\phi)\cos(\phi)C_s, \tag{20}$$

where ϕ is the angle the major drop axes makes with the x-axis, and C_s a parameter dependent on the location of the drop in the channel, which is 5.699 for our case, where the drop is placed exactly in the center. We have investigated four different viscosity ratios: $\lambda = 0.1, 0.3, 3$ and 10. To evaluate D^{2W}, the deformation in the absence of the walls is simply subtracted from the total deformation in the presence of the walls. The results for these simulations can be seen in Fig. 4a-d, where the deformation for two low capillary numbers, $Ca = 0.05$ and 0.1, is shown. For all viscosity ratios we obtain excellent correspondence, especially for the low confinement ratios. At higher confinement ratio we see a deviation, where we find a larger deformation than the prediction of the small-deformation theory. Similar results were are also found for the case with $\lambda = 1$ [33]. Here, drop shapes significantly deviate from an ellipsoidal shape, which is inconsistent with the small-deformation theory, that states that drops remain ellipsoidal, regardless of the confinement ratio. Furthermore, the deviation in the absolute value for the $\lambda = 10$ case is also relatively large. No immediate cause for this deviation is identified, although we find that the calculated orientation angle of the drop is quite low for these cases. Changing the orientation angle with only a couple of degrees is sufficient to get an excellent match here. As the rotation angle is calculated from the maximum node-to-node distance on the interface, and the fact that the location of the nodes is discrete, errors are expected. Modifying the Shapira–Haber model, to remove the influence of the rotation angle, might also provide a better fit [12].

4.2. Drop deformation and migration in Poiseuille flow

As a second validation of our model, we compare our data with those of pressure-driven flow of off-center placed drop, reported by [26]. The major drop axis, the migration velocity and the distance of the mass center of the drop to the channel center are monitored in time. Our results are given in Fig. 5, and can be directly compared with Fig. 7 in [26]. A good match is found, and no further discussion of the results is done, as that is conducted in the before-mentioned work.

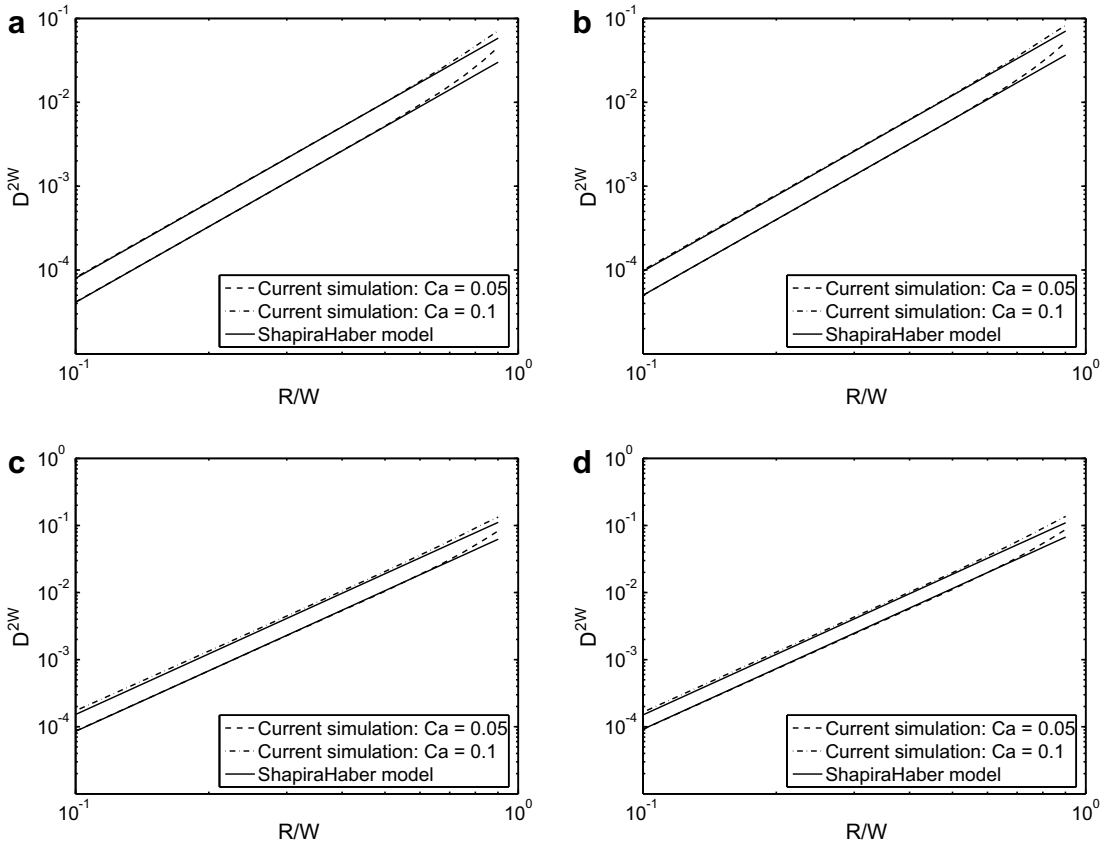

Fig. 4. Comparison of our simulations with the small-deformation theory of [46]: (a) $\lambda = 0.1$, (b) $\lambda = 0.3$, (c) $\lambda = 3$ and (d) $\lambda = 10$.

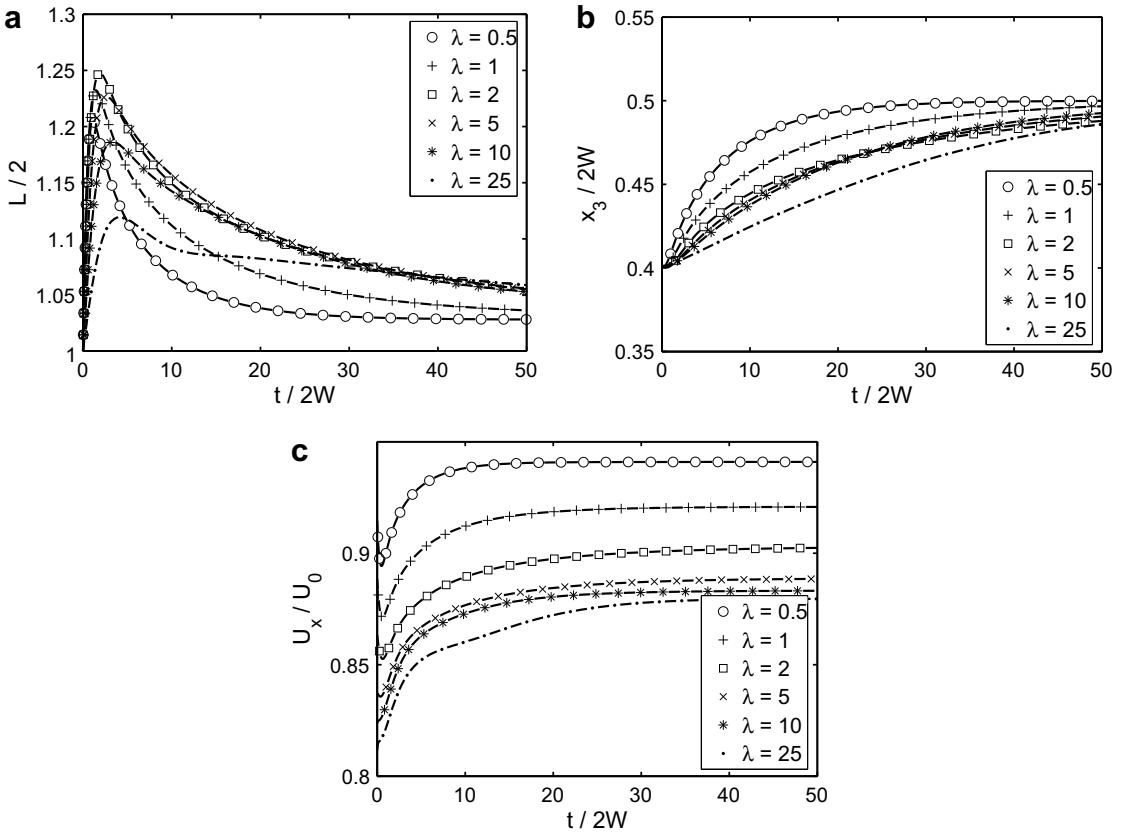

Fig. 5. Evolution of L, z-coordinate of the mass center, and the main migration velocity in the flow direction U in time, with $Ca = 0.5$, $R/W = 0.6$ and the initial location at $z = -0.33$. Results for various viscosity ratios are shown, and can be directly compared with Fig. 7 of [26].

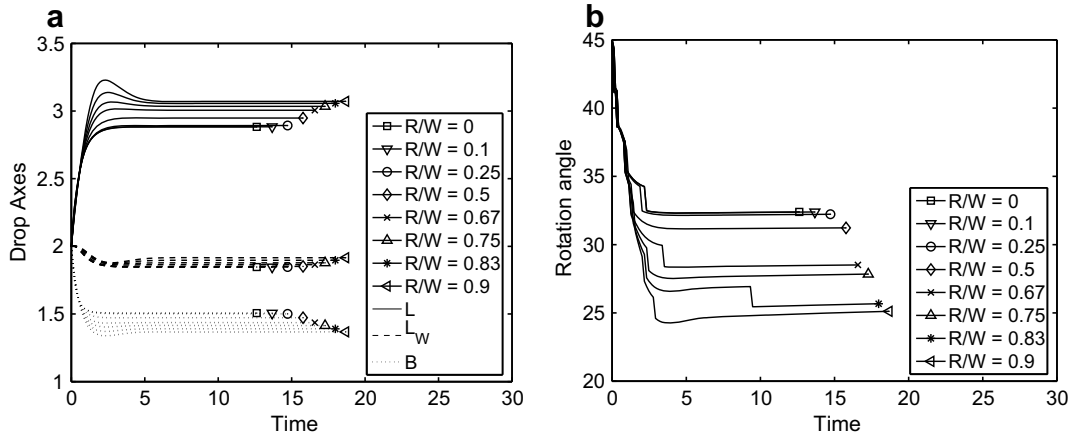

Fig. 6. (a) The major drop axes in time and (b) the rotation angle in time, with $Ca = 0.3$, $\lambda = 0.1$ and various confinement ratios.

4.3. Drop deformation at modest capillary numbers

Next, we consider more profound deformation of drops in shear flow by investigating the deformation with a moderate capillary number. All simulations were started with an initially spherical drop placed in the center of the channel. Simulations were conducted until a steady state was reached. In Fig. 6, the evolution of the major drop axes in time are shown for $Ca = 0.3$, $\lambda = 0.1$ with confinement ratios ranging from 0 to 0.9. The stable drops shapes for $R/W = 0$ and 0.9 can be found in

Fig. 8a and b. The results obtained are similar as those for a viscosity ratio of unity: the deformation increases with increasing confinement ratio. Furthermore, an overshoot in L is seen for the higher confinement ratios, as well as a decrease in the orientation angle, as the drop orients itself more in the flow direction.

The results for $\lambda = 10$ (Figs. 7, 8c and d), however, are different. In this case, the unconfined drop shows an overshoot and damped oscillatory behavior, similar as for highly confined drops for viscosity ratios of $\lambda = 1$ and below. But with increasing the confinement ratio, the overshoot disappears for drops with $\lambda = 10$, although the total deformation is larger. We also see that the orientation angle for the confined drops is higher than for the unconfined. In other words, the walls prevent the drop from aligning itself in the flow direction, or, in the case of high capillary numbers, prevent the drop from tumbling.

4.4. Drop break-up

Finally, we show break up of drops in two situations. In Fig. 9a, some shapes at various instances for a drop with a viscosity ratio of $\lambda = 10$, $Ca = 0.6$ and $R/W = 0.75$ are shown. The remarkable thing is that the drop breaks up. For unconfined drops with a high-viscosity ratio, the rotational component of the shear flow is stronger than the elongational rate [47], lead-

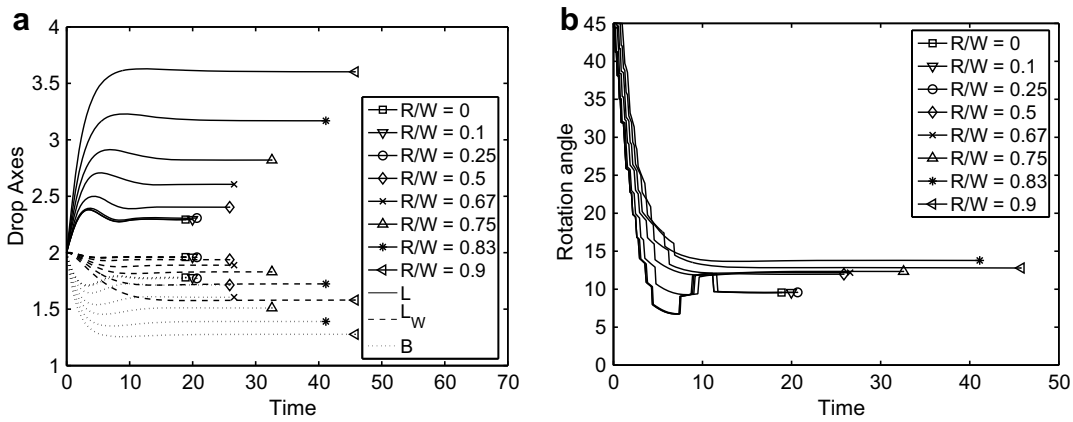

Fig. 7. (a) The major drop axes in time and (b) the rotation angle in time, with $Ca = 0.3$, $\lambda = 10$ and various confinement ratios.

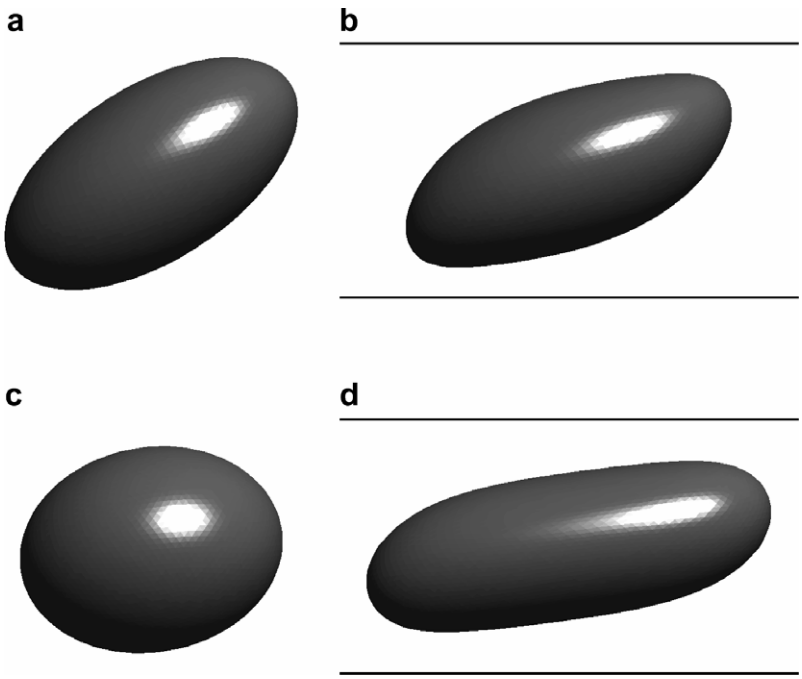

Fig. 8. (a) The steady drop shapes for $Ca = 0.3$, and (a) $\lambda = 0.1$, $R/W = 0$; (b) $\lambda = 0.1$, $R/W = 0.9$; (c) $\lambda = 10$, $R/W = 0$ and (d) $\lambda = 10$, $R/W = 0.9$.

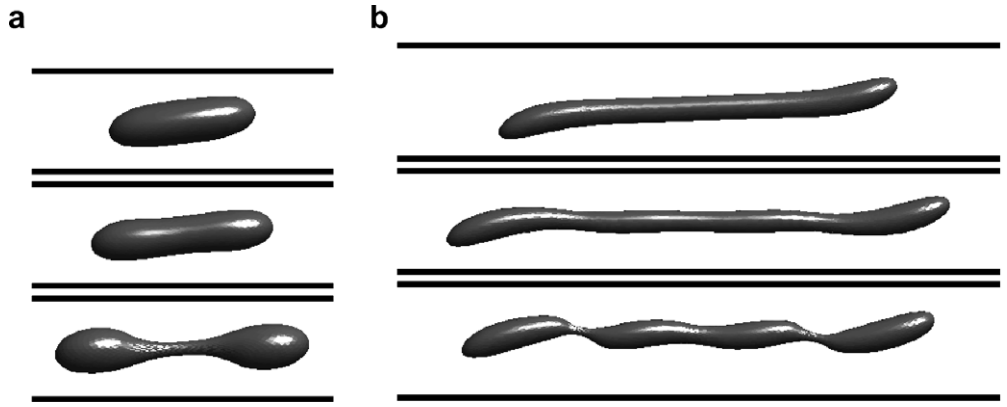

Fig. 9. Breakup modes for confined drops: (a) $Ca = 0.6$, $\lambda = 10$, $R/W = 0.75$; (b) $Ca = 0.54$, $\lambda = 0.3$, $R/W = 0.6$.

ing to a critical viscosity ratio, above which the drop cannot break up, but keeps tumbling in the flow [48]. In our confined case, the walls prevent the tumbling, and keep the drop more aligned in the direction of the straining component of the shear flow. This eventually leads to break up, if the capillary number is high enough. Bentley and Leal [49] showed experimentally in a four-roll mill, that reducing the rotational component in a flow, (going from shear to elongational flow) decreases the critical capillary number for all viscosity ratios. As for the low-viscosity drop, shown in Fig. 9b with $\lambda = 0.3$, $Ca = 0.54$ and $R/W = 0.6$, the break-up mode is similar as reported for drops with matching viscosities [33]: the drop is initially significantly stretched, after which it retracts and breaks up into 3 or more smaller drops. Experimentally it was observed, that drops with a high-viscosity ratio indeed break up faster in a confined situations than drops in bulk flows; lower viscous drops, on the other hand, were found to have a higher critical capillary number for higher confinement ratios [13]. Indeed, in our case the capillary number for the case shown here, which is slightly above the critical capillary number (for situations starting with a spherical drop) we found ($Ca = 0.53$), is higher than the critical capillary number in the unconfined case ($\sim$0.43 for $\lambda = 0.3$). A simple explanation for this second observation could be given by the observation that the drops in confined situations align themselves more in the flow direction (lower rotation angle), and hence experience a weaker straining flow. Based on this, one would expect that the drops themselves are also shorter, but as can be seen in Fig. 6a, that is not the case.

5. Conclusions

In this work, a boundary-integral method is presented for drop deformation between parallel plates which can handle non-unit viscosity ratio systems. For this, the Green's functions are modified to obey the no-slip condition at the walls. The formulation for the double-layer potential involves partial derivatives of the single-layer potential. These terms are written down, as well as an efficient numerical scheme to evaluate them is discussed. The method is then applied to study the behavior of drops in shear flow between two parallel walls, where the drop has a different viscosity than the matrix fluid. For low capillary numbers we find an excellent match with a small-deformation theory, although there are some deviations at the highest confinement ratios. When investigating moderate capillary numbers, we found that low-viscosity drops behave similar as drops with a viscosity ratio of unity, i.e. enhanced deformation and damped oscillatory behavior at larger confinement ratios. The behavior of high-viscosity drops shows that increasing the confinement ratio hinder rotation of drops, keeping them more aligned with the strain direction, which leads to a larger deformation, but less overshoot in the drop axes. High-viscosity drops can be broken in shear flow this way, while low-viscosity drops show break-up behavior similar to drops with matching viscosity, although we find a higher critical capillary number.

Acknowledgements

This work was sponsored by the Dutch Polymer Institute (project #446). We thank J. Blawzdziewicz and E. Wajnryb for discussion of the far-field asymptotics.

Appendix A. Green's functions for parallel walls

The Green's function applied for a point force in a fluid between two parallel walls were derived by [35]. The expressions are all integrals over q with Bessel function weights. The integrands are defined as follows:

$$t_{1nn}(q,z,z_0) = E_-[-v\cosh(v) + B_+\sinh(v)]w\cosh(w) + E_+[-v\sinh(v) + A_+\cosh(v)]w\sinh(w) + E_+[A_+v\sinh(v) - C_+\cosh(v)]\cosh(w) + E_-[B_+v\cosh(v) - D_+\sinh(v)]\sinh(w), \tag{A.1}$$

$$t_{1np}(q,z,z_0) = E_-[v\sinh(v) - A_-\cosh(v)]w\cosh(w) + E_+[v\cosh(v) - B_-\sinh(v)]w\sinh(w) + E_+[-A_+v\cosh(v) + u^2\sinh(v)]\cosh(w) + E_-[-B_+v\sinh(v) + u^2\cosh(v)]\sinh(w), \tag{A.2}$$

$$t_{1pn}(q,z,z_0) = E_+[-v\sinh(v) + A_+\cosh(v)]w\cosh(w) + E_-[-v\cosh(v) + B_+\sinh(v)]w\sinh(w) + E_-[A_-v\cosh(v) - u^2\sinh(v)]\cosh(w) + E_+[B_-v\sinh(v) - u^2\cosh(v)]\sinh(w), \tag{A.3}$$

$$t_{1pp}(q,z,z_0) = E_+[v\cosh(v) - B_-\sinh(v)]w\cosh(w) + E_-[v\sinh(v) - A_-\cosh(v)]w\sinh(w) + E_-[-A_-v\sinh(v) + C_-\cosh(v) - 2u\tanh(u)\cosh(v)]\cosh(w) + E_+[-B_-v\cosh(v) + D_-\sinh(v) - 2u\coth(u)\sinh(v)]\sinh(w), \tag{A.4}$$

$$r_{1pp}(q,z,z_0) = [-2e^{-u}\cosh(v)/\cosh(u)]\cosh(w) + [-2e^{-u}\sinh(v)/\sinh(u)]\sinh(w), \tag{A.5}$$

where

$$u = qW, \quad v = qz_0, \quad w = qz \tag{A.6}$$

$$A_\pm(u) = u \pm \sinh(u)e^{-u} = u \pm 0.5(1 - e^{-2u}), \tag{A.7}$$

$$B_\pm(u) = u \pm \cosh(u)e^{-u} = u \pm 0.5(1 + e^{-2u}), \tag{A.8}$$

$$C_\pm(u) = u(1+u) \pm \sinh(u)e^{-u} = u(1+u) \pm 0.5(1 - e^{-2u}), \tag{A.9}$$

$$D_\pm(u) = u(1+u) \pm \cosh(u)e^{-u} = u(1+u) \pm 0.5(1 + e^{-2u}), \tag{A.10}$$

$$E_\pm(u) = \frac{1}{\sinh(u)\cosh(u) \pm u}. \tag{A.11}$$

The integrands for the pressure vector are

$$p_{1p}(\mathbf{x},\mathbf{x}_0) = E_-[A_-\cosh(v) - v\sinh(v)]\cosh(w) + E_+[B_-\sinh(v) - v\cosh(v)]\sinh(w), \tag{A.12}$$

$$p_{1n}(\mathbf{x},\mathbf{x}_0) = E_-[B_+\sinh(v) - v\cosh(v)]\cosh(w) + E_+[A_+\cosh(v) - v\sinh(v)]\sinh(w). \tag{A.13}$$

For the evaluation of the pressure in the domain, where the pole and the field point have to be switched, they are given by

$$p_{1p}(\mathbf{x}_0,\mathbf{x}) = E_-A_-\cosh(v)\cosh(w) + E_+B_-\sinh(v)\sinh(w) - E_-\cosh(v)w\sinh(w) - E_+\sinh(v)w\cosh(w), \tag{A.14}$$

$$p_{1n}(\mathbf{x}_0,\mathbf{x}) = E_+A_+\sinh(v)\cosh(v) + E_-B_+\cosh(v)\sinh(v) - E_+\sinh(v)w\sinh(v) - E_-\cosh(v)w\cosh(w). \tag{A.15}$$

To recover the free-space Green's function and pressure vector, the integrands are

$$t_{0nn} = t_{0pp} = (1 + q|z - z_0|)\exp(-q|z - z_0|), \tag{A.16}$$

$$t_{0np} = t_{0pn} = -q(z - z_0)\exp(-q|z - z_0|), \tag{A.17}$$

$$r_{0pp} = 2\exp(-q|z - z_0|), \tag{A.18}$$

$$p_{0p}(z,z_0) = \exp(-q|z - z_0|), \tag{A.19}$$

$$p_{0n}(z,z_0) = (-1 + 2H(z - z_0))\exp(-q|z - z_0|), \tag{A.20}$$

with H the Heaviside function.

Appendix B. High q approximations

In Section 2 the high q approximations for t, indicated as $\breve{t}$, are given by

$$\breve{t}_{1nn} = [\{-2(W - z)(W - z_0)\}q^2 + \{-2W + z + z_0\}q - 1]\exp([z + z_0 - 2W]q) + [\{-2(W + z)(W + z_0)\}q^2 + \{-2W - z - z_0\}q - 1]\exp([-z - z_0 - 2W]q) + [\{z - z_0\}q + 1]\exp([-z + z_0 - 4W]q) + [\{-z + z_0\}q + 1]\exp([z - z_0 - 4W]q), \tag{B.1}$$

$$\breve{t}_{1np} = [\{2(W - z)(W - z_0)\}q^2 + \{z - z_0\}q]\exp([z + z_0 - 2W]q) + [\{-2(W + z)(W + z_0)\}q^2 + \{z - z_0\}q]\exp([-z - z_0 - 2W]q) + [\{-z + z_0\}q]\exp([-z + z_0 - 4W]q) + [\{-z + z_0\}q]\exp([z - z_0 - 4W]q), \tag{B.2}$$

$$\breve{t}_{1pn} = [\{-2(W-z)(W-z_0)\}q^2 + \{z-z_0\}q]\exp([z+z_0-2W]q) + [\{2(W+z)(W+z_0)\}q^2 + \{z-z_0\}q]\exp([-z-z_0-2W]q) + [\{-z+z_0\}q]\exp([-z+z_0-4W]q) + [\{-z+z_0\}q]\exp([z-z_0-4W]q), \tag{B.3}$$

$$\breve{t}_{1pp} = [\{2(W-z)(W-z_0)\}q^2 + \{-2W+z+z_0\}q - 1]\exp([z+z_0-2W]q) + [\{2(W+z)(W+z_0)\}q^2 + \{-2W-z-z_0\}q - 1]\exp([-z-z_0-2W]q) + [\{z-z_0\}q + 1]\exp([-z+z_0-4W]q) + [\{-z+z_0\}q + 1]\exp([z-z_0-4W]q), \tag{B.4}$$

$$\breve{r}_{1pp} = -2\exp([z+z_0-2W]q) - 2\exp([-z-z_0-2W]q). \tag{B.5}$$

$$\breve{t}^{(z)}_{1nn} = [\{-2(W-z)(W-z_0)\}q^3 + \{z-z_0\}q^2]\exp([z+z_0-2W]q) + [\{2(W+z)(W+z_0)\}q^3 + \{z-z_0\}q^2] \times \exp([-z-z_0-2W]q) + [\{-z+z_0\}q^2]\exp([-z+z_0-4W]q) + [\{-z+z_0\}q^2]\exp([z-z_0-4W]q), \tag{B.6}$$

$$\breve{t}^{(z)}_{1np} = [\{2(W-z)(W-z_0)\}q^3 + \{-2W+z+z_0\}q^2 + q]\exp([z+z_0-2W]q) + [\{2(W+z)(W+z_0)\}q^3 + \{-2W-z-z_0\}q^2 + q]\exp([-z-z_0-2W]q) + [\{z-z_0\}q^2 + q]\exp([-z+z_0-4W]q) + [\{-z+z_0\}q^2 + q]\exp([z-z_0-4W]q), \tag{B.7}$$

$$\breve{t}^{(z)}_{1pn} = [\{-2(W-z)(W-z_0)\}q^3 + \{2W+z-3z_0\}q^2 + q]\exp([z+z_0-2W]q) + [\{-2(W+z)(W+z_0)\}q^3 + \{2W-z+3z_0\}q^2 + q]\exp([-z-z_0-2W]q) + [\{z-z_0\}q^2 + q]\exp([-z+z_0-4W]q) + [\{-z+z_0\}q^2 + q]\exp([z-z_0-4W]q), \tag{B.8}$$

$$\breve{t}^{(z)}_{1pp} = [\{2(W-z)(W-z_0)\}q^3 + \{-4W+z+3z_0\}q^2]\exp([z+z_0-2W]q) + [\{-2(W+z)(W+z_0)\}q^3 + \{4W+z+3z_0\}q^2]\exp([-z-z_0-2W]q) + [\{-z+z_0\}q^2]\exp([-z+z_0-4W]q) + [\{-z+z_0\}q^2]\exp([z-z_0-4W]q), \tag{B.9}$$

$$\breve{r}^{(z)}_{1pp} = -2q\exp([z+z_0-2W]q) + 2q\exp([-z-z_0-2W]q). \tag{B.10}$$

The fast decaying terms for the pressure vector are

$$\breve{p}_{1p}(\mathbf{x},\mathbf{x}_0) = [\{2(W-z_0)\}q - 1]\exp([z+z_0-2W]q) + [\{2(W+z_0)\}q - 1]\exp([-z-z_0-2W]q) + \exp([-z+z_0-4W]q) + \exp([z-z_0-4W]q), \tag{B.11}$$

$$\breve{p}_{1n}(\mathbf{x},\mathbf{x}_0) = [\{2(W-z_0)\}q + 1]\exp([z+z_0-2W]q) - [\{2(W+z_0)\}q + 1]\exp([-z-z_0-2W]q) + \exp([-z+z_0-4W]q) - \exp([z-z_0-4W]q), \tag{B.12}$$

$$\breve{p}_{1p}(\mathbf{x}_0,\mathbf{x}) = [\{2(W-z)\}q - 1]\exp([z+z_0-2W]q) + [\{2(W+z)\}q - 1]\exp([-z-z_0-2W]q) + \exp([-z+z_0-4W]q) + \exp([z-z_0-4W]q), \tag{B.13}$$

$$\breve{p}_{1n}(\mathbf{x}_0,\mathbf{x}) = [\{2(W-z)\}q + 1]\exp([z+z_0-2W]q) - [\{2(W+z)\}q + 1]\exp([-z-z_0-2W]q) + \exp([z-z_0-4W]q) - \exp([-z+z_0-4W]q), \tag{B.14}$$

$$\breve{p}^{(z)}_{1p}(\mathbf{x}_0,\mathbf{x}) = [\{2(W-z)\}q^2 - 3q]\exp([z+z_0-2W]q) - [\{2(W+z)\}q^2 - 3q]\exp([-z-z_0-2W]q) + q\exp([-z+z_0-4W]q) + q\exp([z-z_0-4W]q), \tag{B.15}$$

$$\breve{p}^{(z)}_{1n}(\mathbf{x}_0,\mathbf{x}) = [\{2(W-z)\}q^2 - q]\exp([z+z_0-2W]q) + [\{2(W+z)\}q^2 - q]\exp([-z-z_0-2W]q) + q\exp([z+z_0-4W]q) + q\exp([-z-z_0-4W]q), \tag{B.16}$$

With these definitions of $\breve{t}$, $t-\breve{t}$ is the same as replacing $E_\pm$ in t with $E_\pm - 4\exp(-2u)$. However, this does not work for t_{1pp} and $t^{(z)}_{1pp}$ due to the hyperbolic tangent and cotangent terms. Therefore, we make an addition to t_{1pp} and define it as

$$t_{1pp}(q,z,z_0) = E_+[v\cosh(v) - B_-\sinh(v)]w\cosh(w) + E_-[v\sinh(v) - A_-\cosh(v)]w\sinh(w) + E_-[-A_-v\sinh(v) + C_-\cosh(v) - 2u\tanh(u)\cosh(v)]\cosh(w) + E_+[-B_-v\cosh(v) + D_-\sinh(v) - 2u\coth(u) \times \sinh(v)]\sinh(w) + 8u[1-\tanh(u)]\exp(-2u)\cosh(v)\cosh(w) + 8u[1-\coth(u)]\exp(-2u) \times \sinh(v)\sinh(w). \tag{B.17}$$

With this modification, the substitution of $E_\pm$ gives $t_{1pp} - \breve{t}_{1pp}$. The same applies to $t^{(z)}_{1pp}$, where the terms $\cosh(w)$ and $\sinh(w)$ in the addition need to be replaced by $q\sinh(w)$ and $q\cosh(w)$ respectively.

Appendix C. Derivatives of Green's function

The derivatives of $\mathbf{G}^{2W}$ to x, indicated with $\{\mathbf{G}^{2W}\}^{(x)}$, are given by

$$\{G^{2W}_{xx}\}^{(x)} = \frac{1}{2}\{s\}^{(x)}\int_0^\infty qJ_1(qs)t_{1pp}\,\mathrm{d}q - \frac{1}{2}\left\{\frac{\hat{y}^2-\hat{x}^2}{s^2}\right\}^{(x)}\int_0^\infty J_2(qs)t_{1pp}\,\mathrm{d}q - \frac{1}{2}\frac{\hat{y}^2-\hat{x}^2}{s^2}\{s\}^{(x)}\int_0^\infty (qJ_1(qs) - \frac{2}{s}J_2(qs))t_{1pp}\,\mathrm{d}q - \{s\}^{(x)}\int_0^\infty qJ_1(qs)r_{1pp}\,\mathrm{d}q, \tag{C.1}$$

$$\{G^{2W}_{zz}\}^{(x)} = -\{s\}^{(x)}\int_0^\infty qJ_1(qs)t_{1nn}\,\mathrm{d}q, \tag{C.2}$$

$$\{G^{2W}_{xy}\}^{(x)} = \left\{\frac{\hat{x}\hat{y}}{s^2}\right\}^{(x)}\int_0^\infty J_2(qs)t_{1pp}\,\mathrm{d}q + \frac{\hat{x}\hat{y}}{s^2}\{s\}^{(x)}\int_0^\infty (qJ_1(qs) - \frac{2}{s}J_2(qs))t_{1pp}\,\mathrm{d}q, \tag{C.3}$$

$$\{G^{2W}_{xz}\}^{(x)} = -\left\{\frac{\hat{x}}{s}\right\}^{(x)}\int_0^\infty J_1(qs)t_{1pn}\,\mathrm{d}q - \frac{\hat{x}}{s}\{s\}^{(x)}\frac{1}{2}\int_0^\infty q(J_0(qs) - J_2(qs))t_{1pn}\,\mathrm{d}q, \tag{C.4}$$

$$\{G^{2W}_{zx}\}^{(x)} = -\left\{\frac{\hat{x}}{s}\right\}^{(x)}\int_0^\infty J_1(qs)t_{1np}\,\mathrm{d}q - \frac{\hat{x}}{s}\{s\}^{(x)}\frac{1}{2}\int_0^\infty q(J_0(qs) - J_2(qs))t_{1np}\,\mathrm{d}q. \tag{C.5}$$

The expression for $\{G^{2W}_{xx}\}^{(x)}$ is the same as $\{G^{2W}_{xx}\}^{(x)}$ with $\frac{\hat{y}^2-\hat{x}^2}{s^2}$ replaced by $\frac{\hat{x}^2-\hat{y}^2}{s^2}$, $\{G^{2W}_{yz}\}^{(x)}$ is the same as $\{G^{2W}_{xz}\}^{(x)}$ with $\frac{\hat{x}}{s}\to\frac{\hat{y}}{s}$ (the same change goes for $\{G^{2W}_{zy}\}^{(x)}$), and $\{G^{2W}_{yx}\}^{(x)} = \{G^{2W}_{xy}\}^{(x)}$. For the derivatives to y, all terms $\{\}^{(x)}$ are replaced by $\{\}^{(y)}$, with

$$\begin{aligned}
&\{s\}^{(x)} = \frac{\hat{x}}{s}, \quad \{s\}^{(y)} = \frac{\hat{y}}{s}, \quad \left\{\frac{x}{s}\right\}^{(x)} = \frac{\hat{y}^2}{s^3}, \quad \left\{\frac{x}{s}\right\}^{(y)} = \left\{\frac{y}{s}\right\}^{(x)} = -\frac{\hat{x}\hat{y}}{s^3},\\
&\left\{\frac{y}{s}\right\}^{(y)} = \frac{\hat{x}^2}{s^3}, \quad \left\{\frac{\hat{x}^2-\hat{y}^2}{s^2}\right\}^{(x)} = \frac{4\hat{x}\hat{y}^2}{s^4}, \quad \left\{\frac{\hat{x}^2-\hat{y}^2}{s^2}\right\}^{(y)} = -\frac{4\hat{x}^2\hat{y}}{s^4},\\
&\left\{\frac{\hat{y}^2-\hat{x}^2}{s^2}\right\}^{(x)} = -\frac{4\hat{x}\hat{y}^2}{s^4}, \quad \left\{\frac{\hat{y}^2-\hat{x}^2}{s^2}\right\}^{(y)} = \frac{4\hat{x}^2\hat{y}}{s^4},\\
&\left\{\frac{\hat{x}\hat{y}}{s^2}\right\}^{(x)} = \frac{\hat{y}(\hat{y}^2-\hat{x}^2)}{s^4}, \quad \left\{\frac{\hat{x}\hat{y}}{s^2}\right\}^{(y)} = \frac{\hat{x}(\hat{x}^2-\hat{y}^2)}{s^4}.
\end{aligned} \tag{C.6}$$

References

[1] V. Cristini, Y.-C. Tan, Theory and numerical simulation of droplet dynamics in complex flows – a review, Lab Chip 4 (2004) 257.
[2] H. Stone, A. Stroock, A. Ajdari, Engineering flows in small devices: microfluidics toward a lab-on-a-chip, Annu. Rev. Fluid Mech. 36 (2004) 381.
[3] T. Squires, S. Quake, Microfluidics: fluid physics at the nanoliter scale, Rev. Mod. Phys. 77 (2005) 977.
[4] W. Olbricht, Pore-scale prototypes of multiphase flow in porous media, Ann. Rev. Fluid Mech. 28 (1996) 187.
[5] J. Barbee, G. Cokelet, The Fahraeus effect, Microvascular Res. 3 (1971) 6.
[6] J. Barbee, G. Cokelet, Prediction of blood flow in tubes with diameters as small as 29μ, Microvascular Res. 3 (1971) 17.
[7] K. Migler, String formation in sheared polymer blends: coalescence, breakup, and finite size effects, Phys. Rev. Lett. 86 (2001) 1023.
[8] J. Pathak, M. Davis, S. Hudson, K. Migler, Layered droplet microstructures in sheared emulsions: finite-size effects, J. Colloid Interface Sci. 255 (2002) 391.
[9] J. Pathak, K. Migler, Droplet-string deformation and stability during microconfined shear flow, Langmuir 19 (2003) 8667.
[10] V. Sibillo, G. Pasquariello, M. Simeone, V. Cristini, S. Guido, Drop deformation in microconfined shear flow, Phys. Rev. Lett. 97 (2006) 054502.
[11] A. Vananroye, P. van Puyvelde, P. Moldenaers, Structure development in confined polymer blends: steady-state shear flow and relaxation, Langmuir 22 (2006) 2273.
[12] A. Vananroye, P. van Puyvelde, P. Moldenaers, Effect of confinement on the steady-state behavior of single droplets during shear flow, J. Rheol. 51 (2007) 139.
[13] A. Vananroye, P. van Puyvelde, P. Moldenaers, Effect of confinement on droplet breakup in sheared emulsions, Langmuir 22 (2006) 3972.
[14] D. Harvie, M. Davidson, J. Cooper-White, M. Rudman, A parametric study of droplet formation through a microfluidic contraction: low viscosity Newtonian droplets, Chem. Eng. Sci. 61 (2006) 5149.
[15] Y. Renardy, The effects of confinement and inertia on the production of droplets, Rheol. Acta 46 (2007) 521.
[16] S. van der Graaf, T. Nisisako, C. Schroën, R. van der Sman, R. Boom, Lattice Boltzmann simulations of droplet formation in a T-shaped microchannel, Langmuir 22 (2006) 4144.
[17] S. Mortazavi, G. Tryggvason, A numerical study of the motion of drops in Poiseuille flow. Part 1. Lateral migration of one drop, J. Fluid Mech. 411 (2000) 325.
[18] M. Jensen, H. Stone, H. Bruus, A numerical study of two-phase Stokes flow in an axisymmetric flow-focussing device, Phys. Fluids 18 (2006) 077103.
[19] C. Coulliette, C. Pozrikidis, Flow due to a periodic array of point forces and the motion of small particles within a cylindrical tube of arbitrary cross section, Phys. Fluids 8 (1996) 2019.
[20] C. Coulliette, C. Pozrikidis, Motion of an array of drops through a cylindrical tube, J. Fluid Mech. 358 (1998) 1.
[21] D. Zhang, H. Stone, Drop formation in viscous flows at a vertical capillary tube, Phys. Fluids 9 (1997) 2234.
[22] M. Staben, A. Zinchenko, R. Davis, Motion of a particle between two parallel plane walls in low-Reynolds-number Poiseuille flow, Phys. Fluids 15 (2003) 1711.
[23] M. Staben, K. Galvin, R. Davis, Low-Reynolds-number motion of a heavy sphere between two parallel plane walls, Chem. Eng. Sci. 61 (2006) 1932.

[24] M. Staben, A. Zinchenko, R. Davis, Dynamic simulation of spheroid motion between two parallel plane walls in low-Reynolds-number Poiseuille flow, J. Fluid Mech. 553 (2006) 187.
[25] A. Zinchenko, R. Davis, A boundary-integral study of a drop squeezing through interparticle constrictions, J. Fluid Mech. 564 (2006) 227.
[26] A. Griggs, A. Zinchenko, R. Davis, Low-Reynolds-number motion of a deformable drop between two parallel plane walls, Int. J. Multiphase Flow 33 (2007) 182.
[27] V. Cristini, J. Blawzdziewicz, M. Loewenberg, Drop breakup in three-dimensional viscous flows, Phys. Fluids 10 (1998) 1781.
[28] V. Cristini, J. Blawzdziewicz, M. Loewenberg, An adaptive mesh algorithm for evolving surfaces: simulation of drop breakup and coalescence, J. Comput. Phys. 168 (2001) 445.
[29] A. Zinchenko, R. Davis, Shear flow of highly concentrated emulsions of deformable drops by numerical simulations, J. Fluid Mech. 455 (2002) 21.
[30] A. Zinchenko, R. Davis, Large-scale simulations of concentrated emulsion flows, Philos. T. Roy. Soc. A 361 (2003) 813.
[31] A. Zinchenko, R. Davis, A multipole-accelerated algorithm for close interaction of slightly deformable drops, J. Comput. Phys. 207 (2005) 695.
[32] P. Dimitrakopoulos, Interfacial dynamics in Stokes flow via a three-dimensional fully-implicit interfacial spectral boundary element method, J. Comput. Phys 225 (2007) 408.
[33] P. Janssen, P. Anderson, Boundary-integral method for drop deformation between parallel plates, Phys. Fluids 19 (2007) 043602.
[34] N. Liron, S. Mochon, Stokes flow for a Stokes-let between 2 parallel flat plates, J. Eng. Math. 10 (1976) 287.
[35] R. Jones, Spherical particle in Poiseuille flow between planar walls, J. Chem. Phys. 121 (2004) 483.
[36] I. Bazhlekov, P. Anderson, H. Meijer, Numerical investigation of the effect of insoluble surfactants on drop deformation and breakup in simple shear flow, J. Colloid Interface Sci. 298 (2006) 369.
[37] J. Rallison, A. Acrivos, A numerical study of the deformation and burst of a viscous drop in an extensional flow, J. Fluid Mech. 89 (1) (1978) 191.
[38] C. Pozrikidis, Boundary-Integral and Singularity Methods for Linearized Viscous Flow, Cambridge University Press, Cambridge, 1992.
[39] A. Vananroye, P. Janssen, P. Anderson, P. van Puyvelde, P. Moldenaers, Microconfined droplet deformation: comparison of experimental and numerical results, Phys. Fluids 20 (2008) 013101.
[40] G. Watson, A Treatise on the Theory of Bessel functions, Cambridge University Press, Cambridge, 1966.
[41] S. Bhattacharya, J. Bladwzdziewicz, E. Wajnryb, Far-field approximation for hydrodynamic interactions in parallel-wall geometry, J. Comput. Phys. 212 (2006) 718.
[42] J. Blake, A note on the image system for a Stokeslet in a no-slip boundary, Proc. Camb. Phil. Soc. 70 (1971) 303.
[43] I. Bazhlekov, P. Anderson, H. Meijer, Non-singular boundary-integral method for deformable drops in viscous flows, Phys. Fluids 16 (2004) 1064.
[44] M. Loewenberg, E. Hinch, Numerical simulation of concentrated emulsion in shear flow, J. Fluid Mech. 321 (1996) 395.
[45] A. Zinchenko, M. Rother, R. Davis, A novel boundary-integral algorithm for viscous interaction of deformable drops, Phys. Fluids 12 (1997) 484.
[46] M. Shapira, S. Haber, Low Reynolds number motion of a droplet in shear flow including wall effects, Int. J. Multiphase Flow 16 (1990) 305.
[47] V. Cristini, Y. Renardy, Scalings for drop sizes in shear-driven breakup: non-microfluidic ways to monodisperse emulsions, Fluid Dynam. Mater. Process. 2 (2006) 77.
[48] H. Grace, Dispersion phenomena in high viscosity immiscible fluid systems and application of static mixers as dispersion devices in such systems, Chem. Eng. Commun. 14 (1982) 225.
[49] B. Bentley, L. Leal, An experimental investigation of drop deformation and breakup in steady, two-dimensional linear flows, J. Fluid Mech. 167 (1986) 241.